QUANTUM SIMULATION

Spin-imbalance in a 2D Fermi-Hubbard system

Peter T. Brown,[1] Debayan Mitra,[1] Elmer Guardado-Sanchez,[1] Peter Schauß,[1] Stanimir S. Kondov,[1]* Ehsan Khatami,[2] Thereza Paiva,[3] Nandini Trivedi,[4] David A. Huse,[1] Waseem S. Bakr[1]†

The interplay of strong interactions and magnetic fields gives rise to unusual forms of superconductivity and magnetism in quantum many-body systems. Here, we present an experimental study of the two-dimensional Fermi-Hubbard model—a paradigm for strongly correlated fermions on a lattice—in the presence of a Zeeman field and varying doping. Using site-resolved measurements, we revealed anisotropic antiferromagnetic correlations, a precursor to long-range canted order. We observed nonmonotonic behavior of the local polarization with doping for strong interactions, which we attribute to the evolution from an antiferromagnetic insulator to a metallic phase. Our results pave the way to experimentally mapping the low-temperature phase diagram of the Fermi-Hubbard model as a function of both doping and spin polarization, for which many open questions remain.

Magnetic fields can modify the behavior of strongly correlated condensed matter systems in important ways, even leading to new phases of matter. Well-known examples include superconductors with finite-momentum pairing induced by Zeeman effects and fractional quantum Hall states induced by orbital effects (*1*). Theoretically, a cornerstone model for studying strongly interacting fermions on a lattice is the Fermi-Hubbard model (*2*). The model has been the topic of intense study over several decades because of its potential implications for understanding high-temperature superconductors and other quantum many-body systems (*3*, *4*). The phase diagram of the Fermi-Hubbard model in the presence of a Zeeman field is qualitatively understood at half-filling, with a canted antiferromagnetic state expected at low temperatures (*5*). Much less is known, even on a qualitative level, about the phase diagram away from half-filling, in which the interplay of doping, spin polarization, and strong correlations can lead to rich physics.

The difficulty of numerical simulations of the Fermi-Hubbard model at low temperatures has motivated quantum simulations that use two-component Fermi gases in optical lattices (*6*, *7*). Rapid developments have been achieved by the recent introduction of quantum gas microscopes for fermionic atoms (*8*–*14*). The reduction of density fluctuations in the Mott insulating phase—previously inferred from bulk measurements (*6*, *7*)—has been explicitly revealed. Furthermore, site-resolved measurements probe antiferromagnetic correlations at all distances and sites in the trapped gas directly (*15*–*17*), complementing other techniques that detect these correlations by measuring the fraction of singlets on neighboring sites (*18*), by using Bragg scattering (*19*) or taking advantage of the fluctuation-dissipation theorem (*20*).

In this work, we probed the magnetic response of a two-dimensional (2D) Fermi-Hubbard system using a spin-imbalanced Fermi gas that has so far been studied mostly by theoretical means (*21*–*23*). Thermodynamically, a nonzero polarization corresponds to the introduction of an effective Zeeman field $h = (\mu_\uparrow - \mu_\downarrow)/2$, where $\mu_{\uparrow,\downarrow}$ are the chemical potentials of the two spin components. The system is described by the Hamiltonian $\mathcal{H} = -t\sum_{\langle ij\rangle,\sigma}\left(c^\dagger_{i,\sigma}c_{j,\sigma} + c^\dagger_{j,\sigma}c_{i,\sigma}\right) + U\sum_i n_{i,\uparrow}n_{i,\downarrow} - \bar{\mu}\sum_i(n_{i,\uparrow} + n_{i,\downarrow}) - 2h\sum_i S^z_i$, which characterizes fermions in a periodic potential with on-site interaction U and tunneling matrix element t between neighboring sites. Here, $c^\dagger_{i,\sigma}$ is the creation operator for a fermion with spin σ on site i, $n_{i,\sigma} = c^\dagger_{i,\sigma}c_{i,\sigma}$, $S^z_i = \frac{1}{2}(n_{i,\uparrow} - n_{i,\downarrow})$, and $\bar{\mu}$ is the average chemical potential.

At low temperatures and in the absence of a field, the half-filled Fermi-Hubbard model exhibits isotropic antiferromagnetic correlations along any projection of the spin owing to the SU(2) spin symmetry. The correlations decay exponentially, and the correlation length diverges at zero temperature. A nonzero magnetic field reduces the spin symmetry to U(1), leading to a finite temperature Kosterlitz-Thouless (KT) phase transition to a canted antiferromagnet, where the correlations decay algebraically (Fig. 1A) (*21*). Canting accommodates magnetization along the field while still benefiting from the superexchange interactions by building up long-range antiferromagnetic correlations of the spin components perpendicular to the magnetization. The KT phase transition boundary has been calculated for the Fermi-Hubbard model, but until recently, different methods had large discrepancies (*24*). Even above this boundary, precursor canted correlations are present, and we directly detect them in our experiment. Furthermore, we probe the spin-imbalanced model in the presence of doping, in which theory is challenged by the fermion "sign problem," revealing a nonmonotonic behavior of the local polarization.

We realized the 2D Fermi-Hubbard model using a degenerate mixture of two hyperfine ground states $|\uparrow\rangle$ and $|\downarrow\rangle$ of ^{6}Li in an optical lattice. The global spin-imbalance $P_g = (N_\uparrow - N_\downarrow)/(N_\uparrow + N_\downarrow)$ can be varied continuously from 0 to ≈0.9 by evaporating the gas in the presence of a magnetic gradient, leading to preferential loss of one of the spin states. We work at a scattering length of 448(9) a_0, where a_0 is the Bohr radius, obtained by adjusting a bias magnetic field in the vicinity of a broad Feshbach resonance centered at 690 G (numbers in parentheses are SEM). The imbalanced mixture is prepared in a single layer (*25*) and subsequently loaded adiabatically into a 2D square lattice of depth 10.5(3) E_R, where $t = h \times 450(25)$ Hz. Here, $E_R = h \times 14.66$ kHz is the recoil energy. For these parameters, we obtained $U/t = 8.0(5)$, where strong antiferromagnetic correlations are expected at half-filling in the balanced gas.

Fluorescence images obtained with quantum gas microscopy techniques enable us to identify singly occupied sites in the lattice, regardless of the spin state (*26*). Doubly occupied sites undergo light-assisted collisions and appear empty. We can also identify singly occupied sites where the atoms are projected onto a chosen eigenstate of S^z by illuminating the cloud with a short pulse of resonant light that ejects atoms in the other eigenstate (Fig. 1, B and C). By first converting atoms on doubly occupied sites to deeply bound molecules, we ensure that they are not affected by this light pulse, and they are subsequently lost in light-assisted collisions during imaging. From these images, we extracted the azimuthally averaged density of atoms on singly occupied (s) sites in a particular spin (σ) state $n^s_\sigma(\mathbf{r})$ and the total density $n^s = n^s_\uparrow + n^s_\downarrow$ shown in Fig. 1D for an imbalanced gas. We observed a plateau in n^s over an extended region near the center of the trap, indicating a reduction in compressibility owing to the charge gap. The deviation of n^s from unity within this region is primarily caused by doublon-hole quantum fluctuations, which are non-negligible at our interaction strength. We characterize the local polarization of singly occupied sites in terms of the measured quantities $p^s = (n^s_\uparrow - n^s_\downarrow)/(n^s_\uparrow + n^s_\downarrow)$. This definition coincides with the true polarization in the absence of doubly occupied sites. At the accessible temperatures, the local polarization is constant throughout the central reduced compressibility region.

We measured spin correlators along two different spin projections: parallel to the field (C^z) and orthogonal to it ($C^\perp$). The spin correlator at a displacement $\mathbf{d}$ between two sites is given by $C^\alpha(\mathbf{d}) = 4(\langle S^\alpha_{\mathbf{i}} S^\alpha_{\mathbf{i}+\mathbf{d}}\rangle - \langle S^\alpha_{\mathbf{i}}\rangle\langle S^\alpha_{\mathbf{i}+\mathbf{d}}\rangle)$, where brackets denote an ensemble and azimuthal average.

[1]Department of Physics, Princeton University, Princeton, NJ 08544, USA. [2]Department of Physics and Astronomy, San José State University, San José, CA 95192, USA. [3]Instituto de Fisica, Universidade Federal do Rio de Janeiro, Caixa Postal 68.528, 21941-972 Rio de Janeiro RJ, Brazil. [4]Department of Physics, The Ohio State University, Columbus, OH 43210, USA.
*Present address: Department of Physics, Columbia University, New York, NY 10027, USA.
†Corresponding author. Email: wbakr@princeton.edu

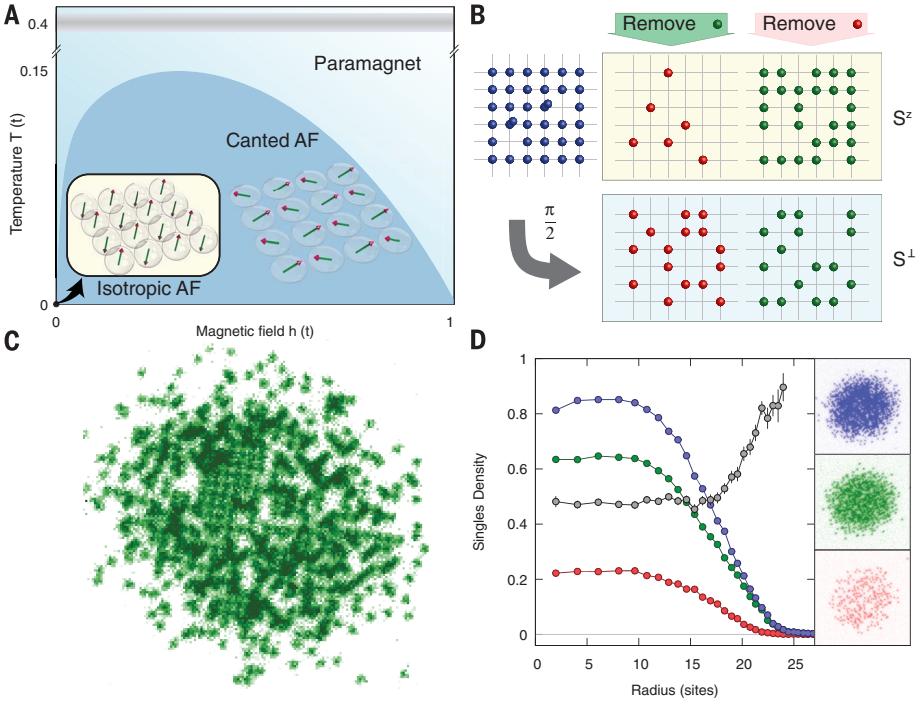

Fig. 1. Site-resolved imaging of a spin-imbalanced Fermi gas in an optical lattice. (**A**) Schematic phase diagram of the 2D Fermi-Hubbard model at half-filling. *T* is the temperature, and *h* is the effective Zeeman field controlled experimentally by the global polarization P_g, both in units of the hopping, *t*. At $h = 0$, the ground state is an antiferromagnet with SU(2) symmetry. For nonzero *h*, there is a finite temperature transition to a canted antiferromagnetic phase. Antiferromagnetic correlations persist at experimental temperatures (gray band). The ellipsoids surrounding the spins illustrate the magnitude of correlations in a given direction. (**B**) We prepare a spin mixture (blue) in an optical lattice then selectively remove one spin state (red or green) and doublons. We extract spin correlations from the resulting density correlations for the S^z spin projection and the $S^\perp$ projection after a global spin rotation (π/2-pulse). (**C**) Site-resolved fluorescence image after removal of one spin state. Field of view is 35 μm. (**D**) Azimuthally averaged profiles and single fluorescence images showing the total singles density n^s (purple), $n^s_\uparrow$ (green), $n^s_\downarrow$ (red), and local polarization p^s (gray) over the trap at $U/t = 8.0(5)$. (Insets) Corresponding exemplary single-shot pictures. Field of view is 48 μm.

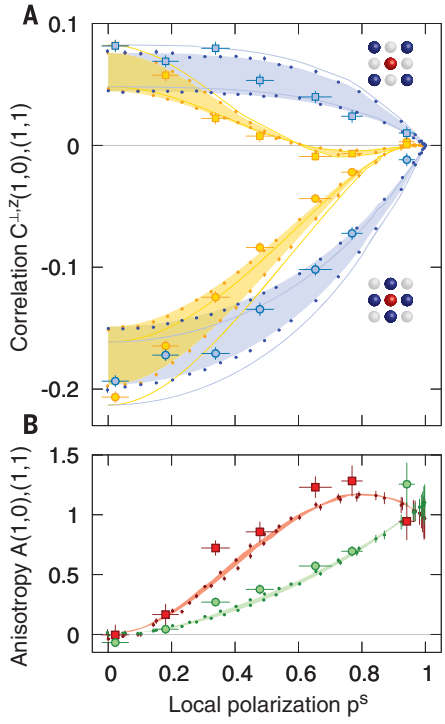

Fig. 2. Anisotropic spin correlations. (**A**) Experimental nearest-neighbor (large circles) and diagonal-neighbor (squares) spin correlations for the S^z (yellow) and $S^\perp$ (blue) spin projections versus local polarization p^s at half-filling. We show NLCE (edges of shading) and DQMC (small circles) results at $U/t = 8$ corrected for our detection efficiency of 0.96 (*26*) and uncorrected NLCE results (solid lines). For the simulations, a temperature band from $T/t = 0.38$ to 0.53 is shown. (**B**) Anisotropy *A* of nearest-neighbor (large green circles) and diagonal-neighbor (red squares) spin correlations with NLCE (solid lines) and DQMC (small circles) results. *A* is insensitive to detection efficiency. Error bars are SEM. Experimental data averaged over ~50 images and azimuthally.

Here, the spin operators are defined for $\alpha = x, y, z$ by $S^\alpha = \frac{1}{2}\begin{pmatrix} c^\dagger_{\mathbf{i},\uparrow} & c^\dagger_{\mathbf{i},\downarrow}\end{pmatrix}\sigma_\alpha\begin{pmatrix} c_{\mathbf{i},\uparrow} \\ c_{\mathbf{i},\downarrow}\end{pmatrix}$, with σ_α being the Pauli matrices. $S^\perp$ is the spin along an undetermined direction in the plane orthogonal to the field, where rotational symmetry ensures $\langle S^\perp\rangle = \langle S^{x,y}\rangle$. $C^z(\mathbf{d})$ is obtained from the singles density correlators $\langle n^s_{\mathbf{i}} n^s_{\mathbf{i}+\mathbf{d}}\rangle$ and $\langle n^s_{\mathbf{i},\sigma} n^s_{\mathbf{i}+\mathbf{d},\sigma}\rangle$, taking into account the effect of doublons and holes (*26*). To extract $C^\perp(\mathbf{d})$, we inserted a radiofrequency pulse to coherently rotate the spins by π/2 before initiating the measurement protocol.

We observed short-range canted antiferromagnetism at half-filling with stronger spin correlations in the direction orthogonal to the magnetization, in contrast to the spin-balanced case in which identical correlations were measured for any projection of the pseudospin. To investigate the dependence of the spin correlations on p^s, we varied the global polarization P_g and extracted the correlations in the half-filled central region. The measured nearest and next-nearest neighbor correlators $C^{\perp,z}$ are shown in Fig. 2A, and the correlator anisotropies, defined as $A = 1 - C^z/C^\perp$, are shown in Fig. 2B. For an almost unpolarized gas, with local polarization $p^s = 0.02(4)$ at half-filling, we found isotropic correlations: $A = -0.06(7)$ for the nearest neighbor and $A = 0.0(2)$ for the next-nearest neighbor. The consistency of these values with zero verifies the SU(2) spin symmetry of the Fermi-Hubbard Hamiltonian at $h = 0$. As the polarization was increased, we observed an overall decrease in correlations, with C^z decreasing faster than $C^\perp$, leading to growing nearest-neighbor anisotropy with polarization.

The system's preference to build correlations in the plane orthogonal to the field can already be understood at the level of a classical Heisenberg model because spins oriented with the staggered magnetization in the *xy* plane can lower their energy by uniformly canting in the direction of the field. In the quantum system, strong quantum fluctuations in two dimensions reduce the magnitude of the nearest-neighbor correlator in the balanced gas from 1 to 0.36 in the ground state (*15*), and thermal fluctuations and imaging fidelity further reduce it to the experimentally measured value of 0.207(4). At nonzero polarization, we observed that the correlator anisotropy is stronger when the sites are further apart. For example, at local polarization $p^s = 0.48(4)$, $A = 0.38(9)$ for the nearest neighbor, whereas $A = 0.8(2)$ for the next-nearest neighbor. The increase of the correlation anisotropy with distance can be partly understood by considering what happens at lower temperatures as we approach the KT transition. There, the $C^\perp$ correlations become long range, whereas the C^z do not, so at long distances, *A* approaches 1.

We compared our measurements to results from Determinantal Quantum Monte Carlo (DQMC) (*27*, *28*) and Numerical Linked Cluster Expansion (NLCE) (*29*, *30*) simulations of the Fermi-Hubbard model at half-filling in the presence of a chemical potential imbalance with the temperature as a free parameter. For the balanced gas, the measured nearest-neighbor correlators give a fitted temperature of $T/t = 0.40(5)$. The temperature increases with polarization, rising to $T/t = 0.57(5)$ at local polarization $p^s = 0.77(3)$. This

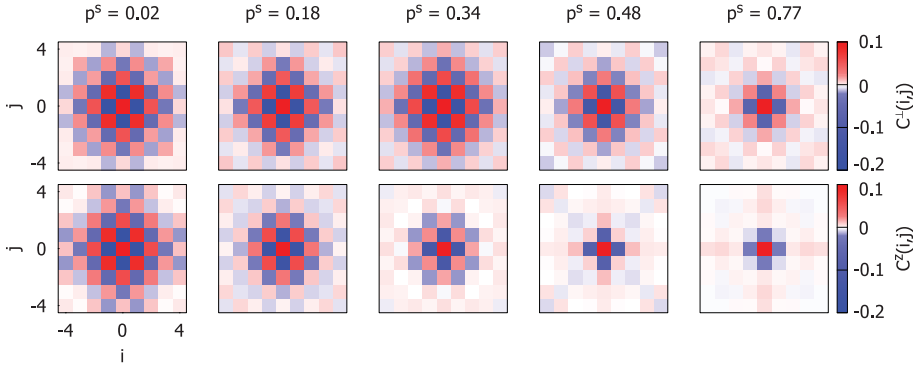

Fig. 3. Spin correlation matrices. Full spin correlation matrices for different site displacements **d** = (*i*,*j*), shown at half-filling for different local polarizations p^s. Top row shows $S^\perp$ correlators, $C^\perp$, and bottom row shows S^z correlators, C^z. Correlator values are averaged over symmetric points. Each panel is calculated from ~50 images. A comparison with NLCE data is provided in (*26*).

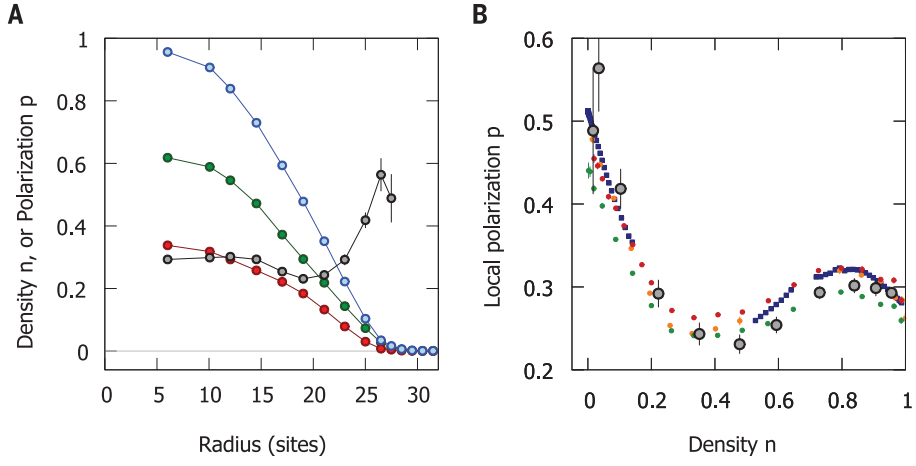

Fig. 4. Nonmonotonic dependence of local polarization on doping at strong interactions. (**A**) Azimuthally averaged density profiles showing the total density n (blue), $n_\uparrow$ (green), $n_\downarrow$ (red), and p (gray) for a spin-imbalanced cloud at U/t = 14.7(8), with global polarization P_g = 0.29(3). (**B**) Local polarization as a function of density (gray circles) assuming linear response. NLCE (blue squares) at U/t = 15 for T/t = 0.35 and h/t = 0.20. DQMC results (small circles) at U/t = 15 for T/t = 0.42 and h/t = 0.22 (red), T/t = 0.36 and h/t = 0.20 (orange), and T/t = 0.42 and h/t = 0.20 (green). Experimental data averaged over ~55 images and azimuthally.

trend may be caused by a reduction of the efficiency of evaporative cooling with increasing spin imbalance. The calculated anisotropy is almost independent of temperature over this range and shows excellent agreement with the experiment (Fig. 2B). The temperatures obtained from the spin correlations agree with those calculated from the singles density correlations (fig. S4).

Insight into the range of the antiferromagnetic order can be gained by examining 2D plots of the spin correlators as a function of the displacement vector between the sites (Fig. 3). The checkerboard pattern is visible for displacements of up to four sites in the almost unpolarized gas, and the overall decrease of all correlations with polarization, as well as the suppression of C^z relative to $C^\perp$, is evident. The $C^\perp$ correlations remain antiferromagnetic at all polarizations, but the C^z correlations can be viewed as the density correlations of the gas of minority spins (*31*) whose modulation becomes longer wavelength as the density of this gas decreases (*26*). This leads to a change in the sign of C^z(1,1) near local polarization p^s = 0.6 (Figs. 2A and 3). The observation of this percent-level negative correlation is only possible because of the superb sensitivity of quantum gas microscopy.

The polarization profile of the imbalanced gas in the trap gives insight into the magnetic susceptibility of the Fermi-Hubbard model in the doped regime [analysis of spin correlations at finite doping is provided in (*26*)]. For strong interactions, we observed that the in-trap polarization profile can exhibit nonmonotonic behavior, as shown in Fig. 4A for U/t = 14.7(8), obtained by increasing the scattering length to 793(12) a_0. For these experiments, we extracted the true local polarization $p = (n_\uparrow - n_\downarrow)/(n_\uparrow + n_\downarrow)$ rather than p^s. The local polarization shows a shallow rise near the edge of the half-filled region then drops in the metallic region, before rising rapidly at the edge of the cloud. These effects can be understood qualitatively in terms of the magnetic susceptibility of the gas at different fillings, $\chi = \frac{1}{n}\frac{\partial\langle S^z\rangle}{\partial h}|_{\tilde{\mu}}$. The field h is constant across the trap because the gas is in chemical equilibrium. Therefore, because we work in the linear regime (*26*), the susceptibility is proportional to the local polarization $\chi = \frac{p}{2h}$. At half-filling (n = 1), the susceptibility is expected to be that of an antiferromagnet $\chi_{AF} \propto 1/J = U/4t^2$, whereas for small doping at our temperatures, there is a nondegenerate gas of holes in the lower Hubbard band and, as a result, a weak maximum in the susceptibility. At intermediate hole doping, the susceptibility crosses over to that of a metal, $\chi_m \propto 1/t$, which is smaller than χ_{AF} for large U/t. Similar behavior has been observed in the cuprates in the normal phase (*32*–*34*) and studied theoretically (*35*, *36*). At even lower filling, the gas is nondegenerate, and there is no filled Fermi sea to hinder spins from aligning with the effective field, leading to an enhanced magnetic susceptibility. We show the polarization versus density in Fig. 4B and compare it with NLCE and DQMC calculations in the local density approximation, which reproduce the nonmonotonic behavior described above. The strength of the field, h/t = 0.21(1), is determined from the polarization at half-filling, which exhibits only a weak dependence on temperatures for $T/t < 0.5$. These calculations are near the limit of these techniques for the doped system, as evidenced by the region from $n \approx 0.2$ to 0.5, where NLCE fails to converge. Comparing DQMC and NLCE in this challenging regime controls for systematic errors (*26*).

Our experimental study of a 2D spin-imbalanced Fermi-Hubbard system is in a regime near the edge of what state-of-the-art numerical techniques can simulate. The high effective fields reached in our experiments allow us to explore canted antiferromagnetic correlations above the KT transition and to observe an interesting dependence of the local polarization on doping. Future directions for both experimental and theoretical work include investigation of spin-imbalance in the attractive 2D Fermi-Hubbard model in which Fulde-Ferrell-Larkin-Ovchinnikov superfluid correlations should be detectable at the entropies achieved in repulsive experiments (*37*) and mapping out the KT transition in the imbalanced repulsive gas phase diagram, which would require lower temperatures. Last, the achievement of cold spin-imbalanced clouds in an optical lattice suggests a route for local entropy reduction by using adiabatic demagnetization cooling, a technique previously demonstrated in bosonic lattice experiments (*38*).

REFERENCES AND NOTES

1. P. Fulde, *Correlated Electrons in Quantum Matter* (World Scientific, 2012).
2. A. Auerbach, *Interacting Electrons and Quantum Magnetism* (Springer, 1994).
3. P. W. Anderson, *Science* **235**, 1196–1198 (1987).
4. P. A. Lee, N. Nagaosa, X.-G. Wen, *Rev. Mod. Phys.* **78**, 17–85 (2006).

5. R. T. Scalettar *et al*., *Phys. Rev. Lett.* **62**, 1407–1410 (1989).
6. R. Jördens, N. Strohmaier, K. Günter, H. Moritz, T. Esslinger, *Nature* **455**, 204–207 (2008).
7. U. Schneider *et al*., *Science* **322**, 1520–1525 (2008).
8. L. W. Cheuk *et al*., *Phys. Rev. Lett.* **114**, 193001 (2015).
9. M. F. Parsons *et al*., *Phys. Rev. Lett.* **114**, 213002 (2015).
10. E. Haller *et al*., *Nat. Phys.* **11**, 738–742 (2015).
11. G. J. A. Edge *et al*., *Phys. Rev. A* **92**, 063406 (2015).
12. A. Omran *et al*., *Phys. Rev. Lett.* **115**, 263001 (2015).
13. R. Yamamoto, J. Kobayashi, T. Kuno, K. Kato, Y. Takahashi, *New J. Phys.* **18**, 023016 (2016).
14. D. Greif *et al*., *Science* **351**, 953–957 (2016).
15. M. F. Parsons *et al*., *Science* **353**, 1253–1256 (2016).
16. M. Boll *et al*., *Science* **353**, 1257–1260 (2016).
17. L. W. Cheuk *et al*., *Science* **353**, 1260–1264 (2016).
18. D. Greif, T. Uehlinger, G. Jotzu, L. Tarruell, T. Esslinger, *Science* **340**, 1307–1310 (2013).
19. R. A. Hart *et al*., *Nature* **519**, 211–214 (2015).
20. J. H. Drewes *et al*., *Phys. Rev. Lett.* **118**, 170401 (2017).
21. A. Koetsier, F. van Liere, H. T. C. Stoof, *Phys. Rev. A* **81**, 023628 (2010).
22. B. Wunsch, L. Fritz, N. T. Zinner, E. Manousakis, E. Demler, *Phys. Rev. A* **81**, 013616 (2010).
23. M. Snoek, I. Titvinidze, W. Hofstetter, *Phys. Rev. B* **83**, 054419 (2011).
24. T. Paiva, R. R. dos Santos, R. T. Scalettar, P. J. H. Denteneer, *Phys. Rev. B Condens. Matter* **69**, 184501 (2004).
25. D. Mitra, P. T. Brown, P. Schauß, S. S. Kondov, W. S. Bakr, *Phys. Rev. Lett.* **117**, 093601 (2016).
26. Materials and methods are available as supplementary materials.
27. R. Blankenbecler, D. J. Scalapino, R. L. Sugar, *Phys. Rev. D Part. Fields* **24**, 2278–2286 (1981).
28. T. Paiva, R. Scalettar, M. Randeria, N. Trivedi, *Phys. Rev. Lett.* **104**, 066406 (2010).
29. M. Rigol, T. Bryant, R. R. P. Singh, *Phys. Rev. Lett.* **97**, 187202 (2006).
30. E. Khatami, M. Rigol, *Phys. Rev. A* **84**, 053611 (2011).
31. E. Batyev, L. Braginskii, *Sov. Phys. JETP* **60**, 781 (1984).
32. J. B. Torrance *et al*., *Phys. Rev. B Condens. Matter* **40**, 8872–8877 (1989).
33. D. C. Johnston, *Phys. Rev. Lett.* **62**, 957–960 (1989).
34. H. Takagi *et al*., *Phys. Rev. B Condens. Matter* **40**, 2254–2261 (1989).
35. R. L. Glenister, R. R. P. Singh, *J. Appl. Phys.* **73**, 6329–6331 (1993).
36. A. Moreo, *Phys. Rev. B Condens. Matter* **48**, 3380–3382 (1993).
37. J. Gukelberger, S. Lienert, E. Kozik, L. Pollet, M. Troyer, *Phys. Rev. B* **94**, 075157 (2016).
38. P. Medley, D. M. Weld, H. Miyake, D. E. Pritchard, W. Ketterle, *Phys. Rev. Lett.* **106**, 195301 (2011).

ACKNOWLEDGMENTS

This work was supported by NSF (grant DMR-1607277), the David and Lucile Packard Foundation (grant 2016-65128), and the Air Force Office of Scientific Research Young Investigator Research Program (grant FA9550-16-1-0269). W.S.B. was supported by an Alfred P. Sloan Foundation fellowship. P.T.B. was supported by the U.S. Department of Defense through the National Defense Science and Engineering Graduate Fellowship Program. E.K. was supported by NSF (grant DMR-1609560). T.P. was supported by Conselho Nacional de Desenvolvimento Científico e Tecnológico, Fundação de Amparo à Pesquisa do Estado do Rio de Janeiro, and Instituto Nacional de Ciência e Tecnologia de Informação Quântica. N.T. acknowledges funding from NSF (grant DMR1309461). We thank M. Rigol for providing exact diagonalization results for the imbalanced system at $U = 0$ to benchmark the NLCE. The data that support the plots presented in this paper and other findings of this study are available from the corresponding author upon reasonable request. The authors declare no competing financial interests.

SUPPLEMENTARY MATERIALS

www.sciencemag.org/content/357/6358/1385/suppl/DC1
Supplementary Text
Figs. S1 to S8
References (*39*–*44*)

16 January 2017; accepted 24 August 2017
10.1126/science.aam7838

Spin-imbalance in a 2D Fermi-Hubbard system

Peter T. Brown, Debayan Mitra, Elmer Guardado-Sanchez, Peter Schauß, Stanimir S. Kondov, Ehsan Khatami, Thereza Paiva, Nandini Trivedi, David A. Huse and Waseem S. Bakr

Science **357** (6358), 1385-1388.
DOI: 10.1126/science.aam7838

Imaging a microscopic power struggle

Strongly interacting fermions in a two-dimensional lattice form a checkerboard pattern, with spins of opposite directions occupying neighboring sites of the lattice. When an external magnetic field is applied, the situation becomes more complicated—should the spins align with the field, or try to preserve the checkerboard order? Brown *et al.* studied this problem using ^{6}Li atoms in an optical lattice with unequal numbers of two spin components; the imbalance between the two played the role of an effective magnetic field. With the field applied, the checkerboard pattern correlations of the spin component perpendicular to the field became stronger than those of the spin component parallel to the field, indicating that the system was approaching the so-called canted antiferromagnetic state.

Science, this issue p. 1385